





Enhanced hydrogen generation by reverse spillover effects over bicomponent catalysts

Zhe Gao ^{1,2}✉, Guofu Wang^{1,2}, Tingyu Lei ¹, Zhengxing Lv³, Mi Xiong^{1,2}, Liancheng Wang^{1,2}, Shuangfeng Xing^{1,2}, Jingyuan Ma³, Zheng Jiang ³ & Yong Qin ^{1,2}✉

The contribution of the reverse spillover effect to hydrogen generation reactions is still controversial. Herein, the promotion functions for reverse spillover in the ammonia borane hydrolysis reaction are proven by constructing a spatially separated NiO/Al₂O₃/Pt bicomponent catalyst via atomic layer deposition and performing in situ quick X-ray absorption near-edge structure (XANES) characterization. For the NiO/Al₂O₃/Pt catalyst, NiO and Pt nanoparticles are attached to the outer and inner surfaces of Al₂O₃ nanotubes, respectively. In situ XANES results reveal that for ammonia borane hydrolysis, the H species generated at NiO sites spill across the support to the Pt sites reversely. The reverse spillover effects account for enhanced H₂ generation rates for NiO/Al₂O₃/Pt. For the CoO_x/Al₂O₃/Pt and NiO/TiO₂/Pt catalysts, reverse spillover effects are also confirmed. We believe that an in-depth understanding of the reverse effects will be helpful to clarify the catalytic mechanisms and provide a guide for designing highly efficient catalysts for hydrogen generation reactions.

¹State Key Laboratory of Coal Conversion, Institute of Coal Chemistry, Chinese Academy of Sciences, Taiyuan 030001, China. ²Center of Materials Science and Optoelectronics Engineering, University of Chinese Academy of Sciences, Beijing 100049, China. ³Shanghai Synchrotron Radiation Facility, Shanghai Advanced Research Institute, Chinese Academy of Sciences, Shanghai 201204, China. ✉email: gaozhe@sxicc.ac.cn; qinyong@sxicc.ac.cn

The ever-increasing global energy demand and the detrimental effect of the CO₂ product of fossil fuels have triggered a widespread search for alternative energy sources, which are effective and renewable and do not cause further environmental issues¹. Because of its high energy density and renewability, H₂ has been regarded as an attractive green fuel and a promising energy carrier for the future to meet increasing energy and environmental challenges². Catalytic H₂ generation from hydrogen storage materials is considered a potential method of H₂ production if they can be effectively catalyzed^{3,4}. The search for efficient catalytic systems would be greatly facilitated by a clearer understanding of the underlying chemical process.

Noble metal catalysts, such as Pt, Pd, and Ru, have been recognized as important classes of catalysts for hydrogen generation, due to their high catalytic activity and durability^{5–11}. It is noted that coupling metal catalysts with secondary metals^{12–15} and/or transition metal oxides^{16–25} is an encouraging strategy to further enhance catalytic performance. In the past, various theories (e.g., the metal-oxide interfacial sites, electron interactions, or hydrogen reverse spillover effect) have been offered to explain the enhancement of H₂ generation when different components are combined in a catalyst. For example, Francisco Zaera and coworkers argued that in the photocatalytic production of H₂ from water with semiconductor catalysts, the role of metal additives is a reverse spillover effect, not to trap excited electrons²⁶. Hydrogen reverse spillover, as a form of spillover, involves the migration of adsorbed hydrogen atoms from an oxide (or other nonmetal surface) to a metal, where they recombine to molecular hydrogen^{27–29}. However, due to the lack of well-defined catalysts with clearly separated functional components and the difficulties in performing in situ characterization technologies, researchers have not formed an agreement on the enhancement mechanism. It is still a challenging issue to reveal the promotion effects of reverse spillover in H₂ generation reactions.

In this work, taking the ammonia borane (NH₃·BH₃, AB) hydrolysis reaction as an example, the promotion functions of reverse spillover in this reaction are proven using a spatially separated NiO/Al₂O₃/Pt catalyst as a model catalyst, in combination with in situ quick XANES characterization. The NiO/Al₂O₃/Pt catalyst was prepared by a facile and general template-assisted atomic layer deposition (ALD) method^{30–36}. In situ XANES results clearly reveal that for H₂ generation from AB, the H species generated at NiO sites spill across the support to the Pt sites, i.e., reverse spillover phenomenon. This accounts for the enhanced H₂ generation rates of bicomponent oxide-metal catalysts, compared with single component Pt-based catalysts. The reverse spillover effects are also confirmed for the CoO_x/Al₂O₃/Pt and NiO/TiO₂/Pt catalysts. Our study provides a guide for designing highly efficient catalysts for hydrogen generation reactions.

Results and discussion

Synthesis and characterization of the catalysts. The NiO/Al₂O₃/Pt catalyst was synthesized by ALD using carbon nanocoils (CNCs) as templates (Supplementary Fig. 1). First, Pt nanoparticles (20 ALD cycles) and an Al₂O₃ film (50 ALD cycles) were deposited onto CNCs. The CNC templates were then removed by calcination. Finally, NiO nanoparticles (100 ALD cycles) were deposited, obtaining NiO/Al₂O₃/Pt, Al₂O₃/Pt and NiO/Al₂O₃ were also produced as reference catalysts.

Figure 1a shows transmission electron microscopy (TEM) image of NiO/Al₂O₃/Pt. Hollow Al₂O₃ nanotubes with a uniform wall thickness (ca. 7 nm) can be clearly observed. The lattice distance of Pt nanoparticles was measured to be ~0.226 nm (Supplementary Fig. 2), which corresponds to the Pt(111) plane. High-angle annular dark field scanning transmission electron microscopy (HAADF-STEM) image and energy-dispersive X-ray

spectroscopy (EDX) mapping (Fig. 1d, e) for NiO/Al₂O₃/Pt show that Ni and Pt are distributed on the outer and inner surfaces of Al₂O₃ nanotubes, respectively. The STEM image, EDX mapping, and line-scanning profile for a cross-sectional specimen prepared by focused ion beam milling along the vertical direction of the Al₂O₃ nanotubes (Supplementary Fig. 3) further demonstrate the separated structure of NiO/Al₂O₃/Pt. TEM images of the Al₂O₃/Pt and NiO/Al₂O₃ catalysts are shown in Fig. 1b, c. There are no Pt particles on the outer surfaces of Al₂O₃ nanotubes for Al₂O₃/Pt (Supplementary Fig. 4). Due to the small size and low contrast of NiO nanoparticles, it is not straightforward to distinguish NiO nanoparticles in Fig. 1a, c. From the HRTEM image of NiO/Al₂O₃ (inset in Fig. 1c), NiO nanoparticles can be clearly observed. The Pt content in the catalysts was measured using inductively coupled plasma-atomic emission spectrometry (ICP-AES) to be 3.65 and 4.23% for NiO/Al₂O₃/Pt and Al₂O₃/Pt, and the Ni content was measured to be 8.05 and 8.71% for NiO/Al₂O₃/Pt and NiO/Al₂O₃, respectively. The N₂ sorption isotherms for the NiO/Al₂O₃, Al₂O₃/Pt, and NiO/Al₂O₃/Pt catalysts almost overlap (Fig. 1f). The Brunauer–Emmett–Teller (BET) surface areas for the NiO/Al₂O₃, Al₂O₃/Pt, and NiO/Al₂O₃/Pt catalysts were calculated to be 95.4, 93.6, and 98.0 m² g⁻¹, respectively. Their pore volumes were 0.34, 0.34, and 0.39 cm³ g⁻¹, respectively. The Barrett–Joiner–Halenda (BJH) pore size distribution curves (Fig. 1g) deduced from desorption branches of the N₂ sorption isotherms confirm that NiO/Al₂O₃, Al₂O₃/Pt, and NiO/Al₂O₃/Pt samples are made up of pores with average sizes centred at 54.9, 54.4, and 57.0 nm, respectively. The pore sizes of these catalysts, i.e., the inner diameters of the Al₂O₃ nanotubes, correspond to the diameters of the CNC sacrificial templates. These results show that all the catalysts possess similar pore structures.

The X-ray photoelectron spectroscopy (XPS) results reveal the existence of Ni²⁺ species in NiO/Al₂O₃ and NiO/Al₂O₃/Pt (Fig. 1h). The XPS peaks for the two catalysts are similar. The XPS peaks located at binding energies of 856.1 and 874.0 eV are attributed to Ni 2p_{3/2} and Ni 2p_{1/2}, respectively, and the peaks located at binding energies of 861.8 and 879.7 eV are attributed to satellite peaks. From the X-ray diffraction (XRD) patterns for the Al₂O₃/Pt and NiO/Al₂O₃/Pt catalysts (Supplementary Fig. 5), the presence of Pt nanoparticles can be confirmed. No diffraction peak assigned to NiO is detected from the XRD patterns for NiO/Al₂O₃ and NiO/Al₂O₃/Pt, which can be ascribed to the high dispersion of ALD-prepared nanoparticles. Hydrogen temperature programmed reduction (H₂-TPR) was used to study the redox properties of the catalysts (Fig. 1i). The profile obtained for Al₂O₃/Pt displays a principal reduction peak at 385 °C, which can be attributed to Pt interacting with Al₂O₃³⁷. The NiO/Al₂O₃ catalyst exhibits a small shoulder peak at approximately 349 °C and a strong peak centred at 431 °C, corresponding to the reductions of bulk NiO and the NiO interacting with Al₂O₃. In contrast, for NiO/Al₂O₃/Pt, the first H₂ consumption peak (corresponding to the reduction of bulk NiO) shifts from 349 to 326 °C and becomes obvious, and a broadened peak centred at 408 °C (corresponding to the reductions of Pt and NiO interacting with Al₂O₃) can be observed. Quantification of the H₂-TPR curves (Supplementary Table 1) shows that the hydrogen consumed by NiO/Al₂O₃/Pt (1.86 mmol H₂ g⁻¹) is greater than the sum of the hydrogen consumed by Al₂O₃/Pt (0.31 mmol H₂ g⁻¹) and NiO/Al₂O₃ (1.29 mmol H₂ g⁻¹). These results demonstrate that the reduction of NiO species is promoted after Pt addition, which can be attributed to the hydrogen spillover effect^{38–41}. This hydrogen spillover effect is further confirmed from the results of in situ quick XANES experiments under a H₂ atmosphere (0.6 MPa, 80 °C) (Supplementary Figs. 6, 7 and Table 2).

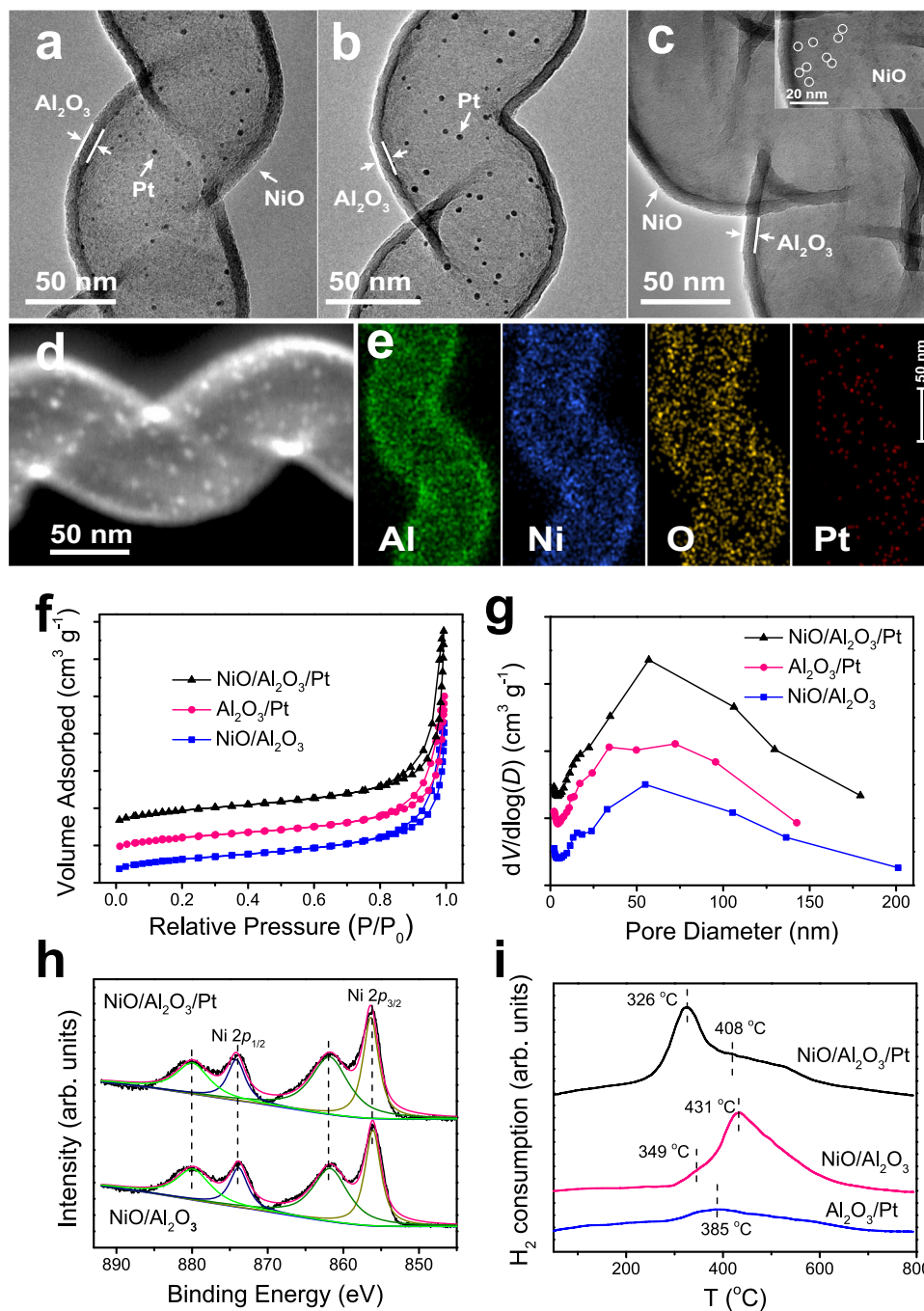


Fig. 1 Structure and chemisorption characterization of the catalysts. TEM images of **a** NiO/Al₂O₃/Pt, **b** Al₂O₃/Pt, and **c** NiO/Al₂O₃ catalysts. Inset in **c** shows a HRTEM image of NiO/Al₂O₃. **d** HAADF-STEM image and **e** EDX elemental mapping of the NiO/Al₂O₃/Pt catalyst. **f** N₂ adsorption–desorption isotherms and **g** the corresponding pore size distributions of the catalysts. **h** XPS Ni 2p analysis of NiO/Al₂O₃ and NiO/Al₂O₃/Pt. **i** H₂-TPR profiles of NiO/Al₂O₃, Al₂O₃/Pt, and NiO/Al₂O₃/Pt.

Enhanced hydrogen generation after NiO addition. Here, the hydrolytic dehydrogenation of AB for H₂ production is selected as a model reaction to investigate the reverse spillover effect. The catalytic performances of different catalysts for the dehydrogenation reaction of AB are shown in Fig. 2. A nearly linear H₂ evolution curve is obtained for Al₂O₃/Pt, suggesting a zero-order reaction with respect to AB (Fig. 2a). For the NiO/Al₂O₃ catalyst, its H₂ evolution curve exhibits a long induction period of approximately 20 min, after which the curve starts to rise gradually. The NiO particles for NiO/Al₂O₃/Pt catalyst is less than that for Al₂O₃/Pt, indicating that NiO and Al₂O₃ are located on the outer surfaces of the Al₂O₃ nanotubes. The reactant molecules (H₂O and AB) easily access the exposed NiO

sites. Thus, the mass transfer in the porous structures is unlikely to lead to the induction period of the NiO/Al₂O₃ catalyst. It is generally believed that new active species are generated during the induction period (Fig. 2b)^{42–44}. However, even after reaction for 60 min, the H₂ evolution volume is still only 3.8 mL, which shows an extremely poor activity for NiO/Al₂O₃. For NiO/Al₂O₃/Pt, a rapid and linear H₂ evolution curve without an induction period is obtained. The time required to complete the hydrolysis reaction for the NiO/Al₂O₃/Pt catalyst is less than that for Al₂O₃/Pt, indicating that NiO addition can greatly enhance the activity of the Al₂O₃/Pt catalyst, even though NiO alone has little activity.

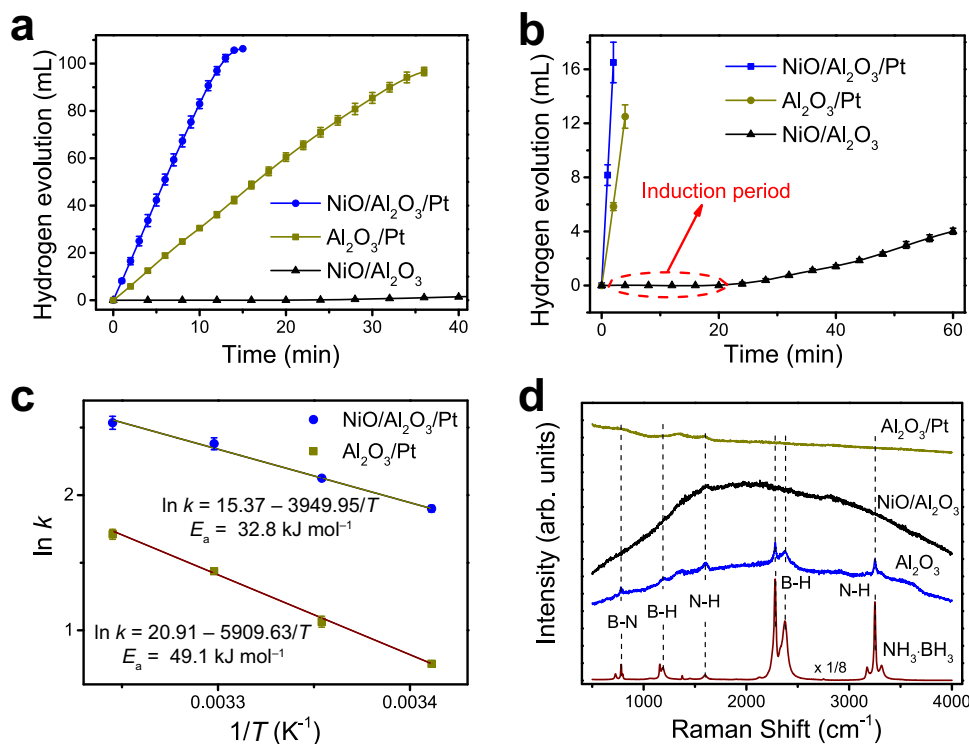


Fig. 2 Catalytic performances of catalysts for the dehydrogenation reaction of AB and Raman spectra for the used catalysts. **a** Volume of H₂ generated from AB solution (0.15 mol L⁻¹) at 25 °C catalyzed by NiO/Al₂O₃, Al₂O₃/Pt, and NiO/Al₂O₃/Pt. **b** The volume of H₂ generated at less than 18 mL versus prolonged time (60 min) clearly shows the induction period for NiO/Al₂O₃. **c** The Arrhenius plots for Al₂O₃/Pt and NiO/Al₂O₃/Pt. Error bars correspond to the standard deviation of three independent measurements. **d** Raman spectra for the used Al₂O₃ support, NiO/Al₂O₃, and Al₂O₃/Pt after reaction for 10 min and data for the reference sample NH₃BH₃.

Kinetic experiments for the Al₂O₃/Pt and NiO/Al₂O₃/Pt catalysts were also conducted. The time dependences for H₂ generation at various temperatures (20–35 °C) were recorded (Supplementary Fig. 8). The catalysts still retain a linear increase in the H₂ generation volume with reaction time. According to Arrhenius plots of ln *k* versus 1/*T* (Fig. 2c), the activation energies (*E*_a) for the hydrolysis of AB using Al₂O₃/Pt and NiO/Al₂O₃/Pt are calculated to be 49.1 and 32.8 kJ mol⁻¹, respectively. The effect of the AB amount on the hydrolysis of AB was investigated (Supplementary Fig. 9). A nearly horizontal relationship in logarithmic plots between the H₂ generation rate and AB concentration is further normalized, indicating that hydrolysis over NiO/Al₂O₃/Pt is also a zero-order reaction with respect to the AB concentration.

The effects of the distance between NiO and Pt components (i.e., the thicknesses of the Al₂O₃ support) and NiO loadings in the catalyst on the catalytic performance were investigated (Supplementary Fig. 10). The synthesis procedures for NiO/100Al₂O₃/Pt, NiO/200Al₂O₃/Pt, and 50NiO/Al₂O₃/Pt are similar to that for NiO/Al₂O₃/Pt, except for adjustment of the ALD cycles for the Al₂O₃ film and NiO nanoparticles (Supplementary Fig. 11). As expected, when the thickness of the Al₂O₃ support increases from 7 nm (NiO/Al₂O₃/Pt, 50 cycles of Al₂O₃) to 13 nm (NiO/100Al₂O₃/Pt, 100 cycles of Al₂O₃) and 25 nm (NiO/200Al₂O₃/Pt, 200 cycles of Al₂O₃), the catalytic activity decreases. As the NiO loading decreases, the H₂ evolution rate also decreases. Even so, the activity of NiO/100Al₂O₃/Pt, NiO/200Al₂O₃/Pt, and 50NiO/Al₂O₃/Pt is still higher than that of the single component Al₂O₃/Pt catalyst.

Catalytic mechanism. Raman measurements were employed to characterize the used catalysts after reaction for 10 min, as shown

in Fig. 2d. The Raman spectrum for the reference sample AB shows the B–N stretching mode at 727 and 783 cm⁻¹, the B–H stretching mode at 2280 and 2375 cm⁻¹, the N–H stretching mode at 3175, 3251, and 3316 cm⁻¹, the BH₃ deformation mode at 1159 and 1188 cm⁻¹, and the NH₃ deformation mode at 1600 cm⁻¹, in agreement with the literature results⁴⁵. For the Al₂O₃ support after reaction, these peaks can still be observed. For the NiO/Al₂O₃ and Al₂O₃/Pt samples after reaction, the NH₃ deformation peak can be found at approximately 1600 cm⁻¹, while the B–N and B–H peaks cannot be observed. These results demonstrate that NiO and Pt can readily dissociate the B–N and B–H bonds of AB in the presence of H₂O.

The dynamic behaviour of Ni species in the catalysts under the H₂ generation reaction was probed with a quick XANES. The incident X-rays usually produce no damage to the material, as opposed to the action of electron or ion probes⁴⁶. This capability of XANES makes it suitable for (in situ) catalyst structure studies⁴⁷. From Fig. 3a, it can be found that the intensity of the white line peak for NiO/Al₂O₃ decreases with the reaction time, indicating that the Ni²⁺ species are gradually reduced. The Ni species are far from being fully reduced after reaction for 60 min. Furthermore, the in situ XANES spectrum was simulated by a linear combination of the ex situ spectrum of the as-prepared catalyst and the spectrum for the reference sample (Ni foil) to quantitatively reveal the dynamic behaviour of Ni species in the catalysts during the reaction. The experimental XANES spectra can be reproduced perfectly by simple linear fitting, with an extremely low R factor (Supplementary Fig. 12 and Supplementary Table 3). The reduction degrees for NiO/Al₂O₃ after reaction for 10, 20, 30, 40, 50, and 60 min are 3.6 ± 0.3, 7.1 ± 0.2, 11.8 ± 0.3, 13.6 ± 0.3, and 14.2 ± 0.2%, respectively (Fig. 3b). The reduction degree does not increase linearly with reaction time.

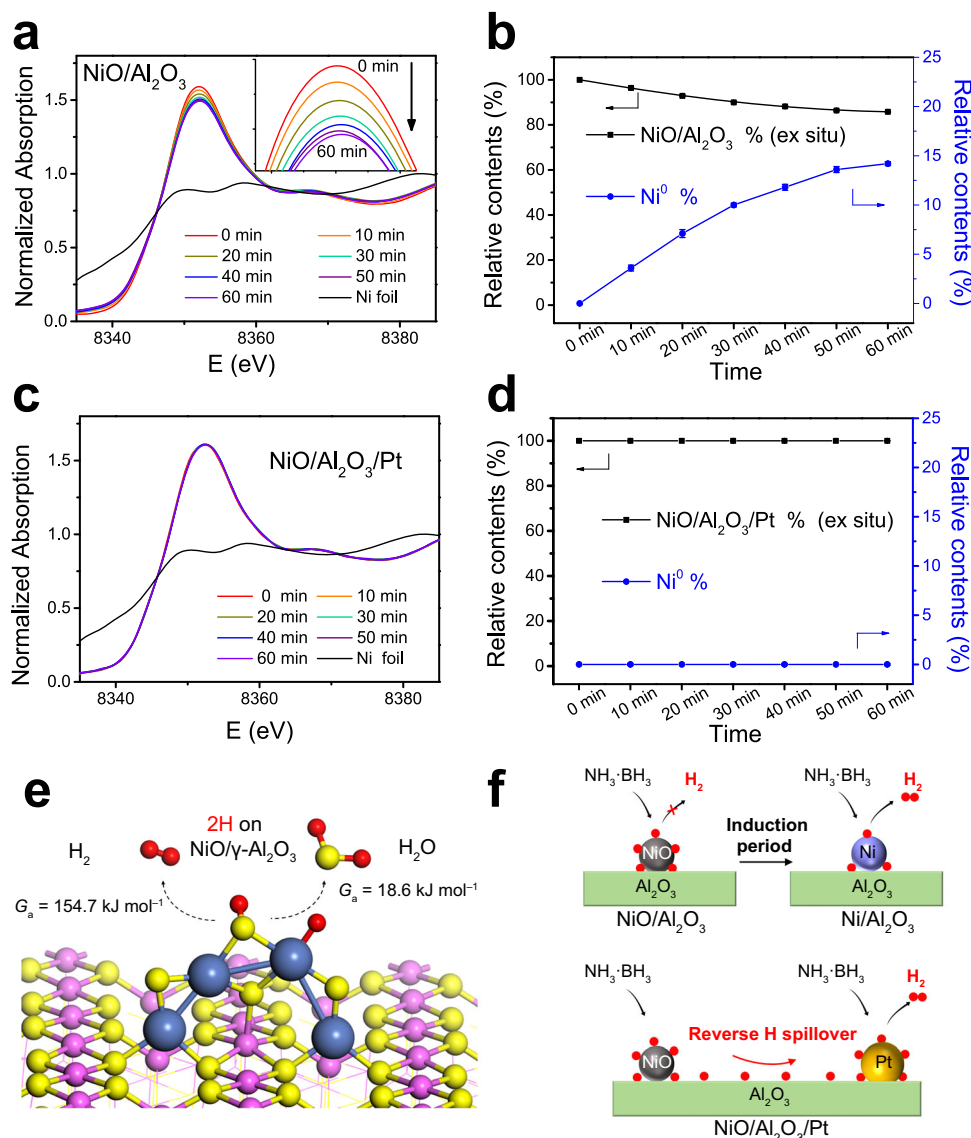


Fig. 3 In situ XANES spectra for the catalysts and proposed mechanisms. In situ Ni K-edge XANES spectra for **a** NiO/Al₂O₃ and **c** NiO/Al₂O₃/Pt, and the percent of metallic Ni⁰ in the **b** NiO/Al₂O₃ and **d** NiO/Al₂O₃/Pt catalysts versus time during the reaction. The inset in **a** shows the expanded sections for the white line peaks. For each sample, the in situ spectrum is fitted by a linear combination of the ex situ spectrum and the spectrum for Ni foil. Error bars represent the fitting errors from XANES. **e** The free energy barriers (G_a) at room temperature (298.15 K) for the formation and desorption of H₂ (left arrow) and water (right arrow) on NiO/γ-Al₂O₃(100) computed by the DFT method. Colour legend: Al, pink; O, yellow; Ni, cyan; and H, red. **f** Proposed reaction mechanisms for NiO/Al₂O₃ and NiO/Al₂O₃/Pt in the H₂ generation reaction. During the induction period for NiO/Al₂O₃, the H species generated at NiO sites are consumed to reduce the oxide catalyst to metallic Ni⁰. For NiO/Al₂O₃/Pt, the H species generated at NiO sites reversely spill across the Al₂O₃ support to Pt sites, where they can combine into H₂ and release.

These results demonstrate that metallic Ni⁰ species are generated gradually during the reaction, and the Ni⁰ generation rate slows down with time. For NiO/Al₂O₃/Pt, one may expect that more NiO will be reduced into metallic Ni⁰ after Pt addition due to spillover effects. Surprisingly, the in situ XANES spectra remain unchanged throughout the reaction, indicating that the reduction of Ni²⁺ species is totally inhibited after Pt addition (Fig. 3c, d).

Discussion

Our results show that the H₂ generation rate for Al₂O₃/Pt for the hydrolysis of AB can be enhanced after NiO addition, even though Pt and NiO are spatially separated by Al₂O₃ support. Here, the promotion functions of reverse spillover in the AB hydrolysis reaction are proven using a spatially separated catalyst

as an ideal model catalyst based on kinetic analyses, Raman, in situ XANES, and DFT calculation results.

The Al₂O₃/Pt catalyst can catalyze the hydrolysis reaction of AB effectively, indicating that reactants can easily diffuse towards Pt sites. Pt nanoparticles for Al₂O₃/Pt are confined in the Al₂O₃ nanotubes. According to the BJH results, the average pore size of the nanotubes is larger than 50 nm, which is the main channel for the diffusion of reaction molecules to Pt sites. The Raman results demonstrate that Pt can readily dissociate the B–N and B–H bonds for AB in the presence of H₂O, while the Al₂O₃ support cannot. Then, the generated H species are easily released from the Pt surface⁴⁸.

The NiO/Al₂O₃ catalyst shows poor activity in the hydrolysis reaction. However, the Raman results demonstrate that NiO can also dissociate the B–N and B–H bonds of AB in the presence of

H₂O, generating H species. It is believed that NiO facilitates the adsorption of H–OH and the dissociation of electropositive H, which favours the attack of electronegative H in AB¹⁸. The H species generated at NiO sites can either be released as H₂ from the oxide surface or can be consumed to reduce the NiO catalyst to metallic Ni⁰. The formation and desorption free energies for H₂ and H₂O on NiO sites in an aqueous environment were calculated using the DFT method (Fig. 3e and Supplementary Fig. 13). The free energy barrier (G_a) at room temperature (298.15 K) for the formation of H₂ is 154.7 kJ mol⁻¹, whereas a much lower free energy barrier of 18.6 kJ mol⁻¹ is required for H₂O formation. This indicates that the H species tend to be consumed to reduce the NiO catalyst to form H₂O. At the induction period for the H₂ evolution curve for NiO/Al₂O₃, no H₂ is produced, confirming that the H species are not released from the oxide surface. The in situ XANES results indicate that the generated H species are consumed for slowly reducing the oxide catalyst to metallic Ni⁰, which is consistent with the DFT results. After metallic Ni⁰ is produced, then the generated H species can be released from the metal surface (Fig. 3f).

For the spatially separated NiO/Al₂O₃/Pt catalyst, its H₂ generation rate for the hydrolysis of AB is enhanced. The in situ XANES results indicate that no metallic Ni⁰ is observed in the NiO/Al₂O₃/Pt catalyst during the AB hydrolysis reaction, while reduction is observed in the NiO/Al₂O₃ catalyst. For both NiO/Al₂O₃ and NiO/Al₂O₃/Pt, NiO particles are located on the outer surfaces of Al₂O₃ nanotubes. N₂ sorption isotherm results show that these two samples possess similar pore structures. Thus, the different reduction behaviours of NiO species for NiO/Al₂O₃ and NiO/Al₂O₃/Pt during the AB hydrolysis reactions are unlikely to be due to the mass transfer in the porous structures. The Raman results demonstrate that H species are generated at NiO and Pt sites at the same time. The H species generated at NiO sites can be released as H₂ from the NiO surface, consumed to reduce NiO, or released from Pt sites through reverse spillover. Generally, the desorption of H₂ molecules on Pt sites is quite easy and is considered to be barrier free^{49,50}. Thus, reverse spillover is the lowest energy pathway. This is also confirmed experimentally. The H₂ evolution curve for NiO/Al₂O₃ confirms that the H species are not released from NiO. The reduction of NiO is totally inhibited after Pt addition, revealing that the H species generated at NiO sites are not consumed for the reduction of NiO. The H species spill across the Al₂O₃ support from NiO to Pt sites, where they can combine into H₂ and release (Fig. 3f). This is called the reverse spillover process, which accounts for the enhanced H₂ generation rate for NiO/Al₂O₃/Pt after NiO addition.

The reverse spillover phenomenon has also been confirmed in other catalytic systems, for example, in AB hydrolysis catalyzed by CoO_x/Al₂O₃/Pt. As shown in Fig. 4a, an induction period can also be found in the H₂ evolution curve for the CoO_x/Al₂O₃ catalyst. For CoO_x/Al₂O₃/Pt, a rapid and nearly linear H₂ evolution curve is obtained, and its activity is higher than that of Al₂O₃/Pt. From the in situ XANES results, it can be found that after reaction for 30 min, the position of the white line peak for CoO_x/Al₂O₃ shifts to a lower energy, and the intensity of the white line peak decreases, indicating that the Co oxide species are reduced (Fig. 4b). For CoO_x/Al₂O₃/Pt, the change in the white line peak after the reaction is very slight (Fig. 4c). The in situ XANES spectrum was simulated by a linear combination of the ex situ spectrum for the as-prepared catalyst and the spectra obtained for the reference samples (CoO and metallic Co⁰) (Supplementary Fig. 14). For CoO_x/Al₂O₃ after reaction for 30 min, 9.9% extra CoO and 12.9% extra metallic Co⁰ are formed. However, for CoO_x/Al₂O₃/Pt, 9.7% of extra CoO and only 1.6% of extra metallic Co⁰ are formed. It can be concluded that the

reduction of Co oxide species to metallic Co⁰ is mostly inhibited after Pt addition.

In addition to nonreducible Al₂O₃, when reducible TiO₂ is used as a support, reverse spillover effects are also confirmed (Supplementary Figs. 15 and 16). As shown in Fig. 4d, the induction period in the H₂ evolution curve for the NiO/TiO₂ catalyst is shortened to 7 min, indicating that NiO supported on TiO₂ is easier to reduce than that supported on Al₂O₃. The H₂ evolution curve for NiO/TiO₂/Pt is not linear. In the beginning, its rate is similar to that of TiO₂/Pt. After that, the rate for NiO/TiO₂/Pt begins to increase rapidly, exceeding the rate for TiO₂/Pt. This implies that NiO sites are reduced to metallic Ni⁰ sites during the reaction. The in situ XANES spectra for NiO/TiO₂ and NiO/TiO₂/Pt are slightly rough, which is due to the high activities of the catalysts. The liquid reaction system is disturbed by a large amount of H₂ bubbles, and thus, the X-ray absorption is affected. The in situ XANES (Fig. 4e, f) and its linear combination fitting results (Supplementary Fig. 17) demonstrate that for NiO/TiO₂ after reaction for 30 min, 26.1% extra metallic Ni⁰ is formed, while for NiO/TiO₂/Pt, 13.0% extra metallic Ni⁰ is formed. The reduction of NiO to metallic Ni⁰ is partially inhibited after Pt addition because of the reverse spillover effects. There are two competing pathways for the H species generated at the NiO sites of NiO/TiO₂/Pt. A fraction of the H species spill over reversely to Pt sites; the rest is consumed to reduce NiO to metallic Ni⁰.

In summary, we designed spatially separated NiO/Al₂O₃/Pt catalysts to clarify the contribution of the reverse spillover effect to enhanced H₂ generation rates. The in situ XANES results reveal that the H species generated at NiO sites are not consumed for the reduction of NiO to Ni⁰ or released as H₂ at NiO sites. Instead, they reversely spill across the support to the Pt sites. The reverse spillover effects account for the enhanced H₂ generation rates. The effects are also confirmed for CoO_x/Al₂O₃/Pt and NiO/TiO₂/Pt catalysts. In general, we believe that, with the help of an in-depth understanding of reverse spillover effects, this work can provide guidance for rationally designing highly efficient catalysts for H₂ production in the future.

Methods

Synthesis of Al₂O₃/Pt catalysts. Typically, Pt nanoparticles (20 cycles) were deposited onto the CNC templates by ALD. Subsequently, the as-prepared Pt/CNCs were coated by an Al₂O₃ support film (50 cycles). Then, the CNC templates were removed by calcination at 500 °C for 1 h, obtaining an Al₂O₃/Pt catalyst.

Synthesis of NiO/Al₂O₃/Pt and CoO_x/Al₂O₃/Pt catalysts. To obtain NiO/Al₂O₃/Pt, NiO nanoparticles (100 cycles) were deposited onto Al₂O₃/Pt by ALD. The deposition cycles for NiO nanoparticles (50 and 100 cycles) and Al₂O₃ film (50, 100, and 200 cycles) can be adjusted, obtaining 50NiO/Al₂O₃/Pt, NiO/100Al₂O₃/Pt, and NiO/200Al₂O₃/Pt. To obtain CoO_x/Al₂O₃/Pt, CoO_x nanoparticles (35 cycles) were deposited onto Al₂O₃/Pt by ALD.

Synthesis of NiO/Al₂O₃ and CoO_x/Al₂O₃ catalysts. CNCs were first coated with an Al₂O₃ layer (50 cycles) by ALD and then calcined at 500 °C for 1 h. Next, NiO (100 cycles) or CoO_x (35 cycles) nanoparticles were deposited by ALD, obtaining a NiO/Al₂O₃ or CoO_x/Al₂O₃ catalyst.

Synthesis of NiO/TiO₂, TiO₂/Pt, and NiO/TiO₂/Pt catalysts. CNCs were first coated with a TiO₂ layer (200 cycles) by ALD and calcined at 500 °C for 1 h. Then, NiO (100 cycles) nanoparticles were deposited by ALD, obtaining a NiO/TiO₂ catalyst. To obtain TiO₂/Pt, Pt nanoparticles (20 cycles) and a TiO₂ film (200 cycles) were deposited onto a CNC template. Then, the CNC template was removed by calcination at 500 °C for 1 h, obtaining a TiO₂/Pt catalyst. NiO (100 cycles) nanoparticles were deposited onto TiO₂/Pt, producing NiO/TiO₂/Pt.

Sample characterization. The chemical compositions of these samples were determined by ICP-AES. The TEM and HRTEM images were taken on a JEOL-2100F microscope. The N₂ sorption measurements were performed using

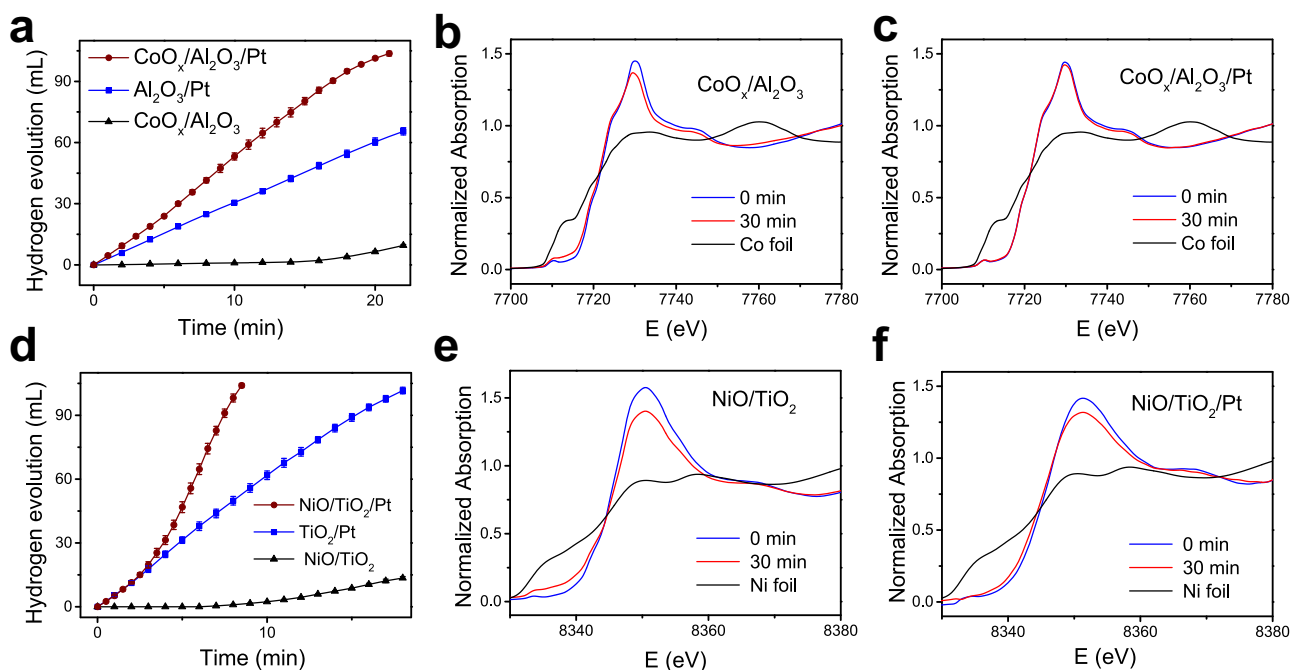


Fig. 4 Reverse spillover effects in AB hydrolysis catalyzed by the $\text{CoO}_x/\text{Al}_2\text{O}_3/\text{Pt}$ and $\text{NiO}/\text{TiO}_2/\text{Pt}$ catalysts. **a** Volume of H_2 generated from AB solution at 25°C catalyzed by $\text{CoO}_x/\text{Al}_2\text{O}_3$, $\text{Al}_2\text{O}_3/\text{Pt}$, and $\text{CoO}_x/\text{Al}_2\text{O}_3/\text{Pt}$. In situ Co K-edge XANES spectra for **b** $\text{CoO}_x/\text{Al}_2\text{O}_3$ and **c** $\text{CoO}_x/\text{Al}_2\text{O}_3/\text{Pt}$ catalysts before reaction and after reaction for 30 min and the spectrum for Co foil. **d** Volume of H_2 generated from AB solution at 25°C catalyzed by NiO/TiO_2 , TiO_2/Pt , and $\text{NiO}/\text{TiO}_2/\text{Pt}$. In situ Ni K-edge XANES spectra for **e** NiO/TiO_2 and **f** $\text{NiO}/\text{TiO}_2/\text{Pt}$ catalysts before reaction and after reaction for 30 min and the spectrum obtained for Ni foil. Error bars correspond to the standard deviation for three independent measurements.

Micromeritics Tristar 3000 at 77 K. XRD patterns were collected on a Bruker D8 Advance X-ray diffractometer using a Cu K α source. XPS spectra were recorded on an AXIS ULTRA DLD spectrometer (Shimadzu/Kratos) to characterize the surface composition with the Al K α line as the excitation source. H_2 -TPR experiments were performed using a tubular quartz reactor (TP-5080, Tianjin Xianquan, China), into which a 50 mg sample was loaded. The reduction was conducted in a 10% H_2/N_2 atmosphere at a heating rate of $10^\circ\text{C}/\text{min}$. Hydrogen consumption was calculated by an external standard method using H_2 -TPR for CuO as the standard. The Raman spectra were performed on a LabRam HR Evolution (Horiba, France) spectrometer employing a He–Ne laser with an excitation wavelength of 532 nm. After the AB catalytic hydrolysis reaction for 10 min, the catalysts were centrifuged and dried in a vacuum oven at 30°C . Finally, the samples were loaded, and the spectra were recorded at room temperature. The in situ XANES for Ni and Co K-edge were obtained on the 1W1B beamline of the Beijing Synchrotron Radiation Facility (BSRF), Institute of High Energy Physics, Chinese Academy of Sciences, and the BL14W1 and BL11B beamlines of the Shanghai Synchrotron Radiation Facility (SSRF), Shanghai Advanced Research Institute, Chinese Academy of Sciences. A Si (111) double-crystal monochromator was used to reduce the harmonic component of the monochrome beam. Ni and Co foil, NiO, CoO, and Co_3O_4 were used as reference samples and measured in transmission mode. The sample wafer was placed in the centre of a homemade in situ XANES cell. The spectra for the catalyst were first collected in transmission mode. After that, the AB solution (5 g L^{-1}) was fed into the reactor at a speed of 5 mL min^{-1} by a sampling pump. The quick XANES were collected during the reaction at different times. IFEFFIT software was used to calibrate the energy scale, to correct the background signal, and to normalize the intensity. The spectra at the edge jump were simulated by a linear function of the reference Ni foil and the NiO-based catalyst before the reaction to estimate the proportion of metallic Ni 0 in the catalyst during the reaction. The following formula was used:

(in situ XANES) = $f_1 \cdot (\text{XANES of Ni foil}) + f_2 \cdot (\text{ex situ XANES})$, where f_1 and f_2 are the fractions of the Ni foil and the as-prepared catalyst before the reaction, respectively.

Catalytic testing. The catalytic performance of the samples was tested for AB hydrolytic dehydrogenation. Typically, the catalysts were first dispersed in deionized water (10 mL) placed in a round bottom flask with a magnetic stirrer at $25 \pm 0.5^\circ\text{C}$. The reaction was initialized by adding 48 mg of AB (Aldrich, 97%) into the reaction flask under stirring (700 rpm). A gas burette filled with water was connected to the flask to measure the amount of hydrogen evolved during the reaction by monitoring the displacement of the water level. In the AB concentration-dependent study, the reaction was performed at different AB

concentrations (75, 112.5, 150, and 187.5 mmol L^{-1}) at $25 \pm 0.5^\circ\text{C}$. To calculate the activation energy (E_a), the reaction temperature was varied in the range of $20\text{--}35^\circ\text{C}$, and the AB concentration was kept constant at 150 mmol L^{-1} .

Computational method. All DFT calculations were carried out using periodic spin-polarized density functional theory with the Perdew–Burke–Ernzerhof generalized gradient approximation functional⁵¹ as implemented in the Vienna ab initio simulation package (VASP)^{52,53}. The calculations were performed using a plane-wave basis set, with a cut-off kinetic energy of 400 eV. Projector-augmented-wave⁵⁴ potentials were used to describe the electron–ion interactions. Dispersion interactions were included by using the DFT–D3 (BJ) correction method of Grimme et al.^{55,56}. The crystal structure of $\gamma\text{-Al}_2\text{O}_3$ proposed by Gutiérrez et al.⁵⁷ was adopted in our model system. The most stable (100) surface of $\gamma\text{-Al}_2\text{O}_3$ with three alumina layers and a Ni_4O_4 cluster adsorbed onto it were used for the NiO/ $\gamma\text{-Al}_2\text{O}_3$ (100) slab model. The two bottom layers of the slab were kept fixed. The thickness of the vacuum region was 20 \AA . A Monkhorst-Pack grid was used for Brillouin-zone integrations with $1 \times 1 \times 1\text{ k-mesh}$ (gamma point) sampling. The solvation effect was included with an implicit solvation solvent of water using the VASPsol tool⁵⁸. The free energies at room temperature (298.15 K) were obtained by adding to the DFT electronic energy (E), the zero-point energy, enthalpy, and entropy contribution from the vibrational modes. The transition states (TS) were calculated using the climbing image nudged elastic band method⁵⁹, and frequency analysis was confirmed to verify the TS.

Data availability

The data that support the findings of this study are available from the corresponding authors upon reasonable request.

Received: 14 April 2021; Accepted: 3 December 2021;

Published online: 10 January 2022

References

- Suh, M. P., Park, H. J., Prasad, T. K. & Lim, D. W. Hydrogen storage in metal-organic frameworks. *Chem. Rev.* **112**, 782–835 (2012).
- Dresselhaus, M. S. & Thomas, I. L. Alternative energy technologies. *Nature* **414**, 332–337 (2001).

- Sun, Q., Wang, N., Xu, Q. & Yu, J. Nanopore-supported metal nanocatalysts for efficient hydrogen generation from liquid-phase chemical hydrogen storage materials. *Adv. Mater.* **32**, 2001818 (2020).
- Schlapbach, L. & Züttel, A. Hydrogen-storage materials for mobile applications. *Nature* **414**, 353–358 (2001).
- Chen, W. et al. Mechanistic insight into size-dependent activity and durability in Pt/CNT catalyzed hydrolytic dehydrogenation of ammonia borane. *J. Am. Chem. Soc.* **136**, 16736–16739 (2014).
- Yang, J. et al. Atomic design and fine-tuning of subnanometric Pt catalysts to tame hydrogen generation. *ACS Catal.* **11**, 4146–4156 (2021).
- Bi, Q. et al. Dehydrogenation of formic acid at room temperature: boosting palladium nanoparticle efficiency by coupling with pyridinic-nitrogen-doped carbon. *Angew. Chem. Int. Ed.* **55**, 11849–11853 (2016).
- Tedsree, K. et al. Hydrogen production from formic acid decomposition at room temperature using a Ag–Pd core-shell nanocatalyst. *Nat. Nanotechnol.* **6**, 302–307 (2011).
- Wang, N. et al. In situ confinement of ultrasmall Pd clusters within nanosized silicalite-1 zeolite for highly efficient catalysis of hydrogen generation. *J. Am. Chem. Soc.* **138**, 7484–7487 (2016).
- Liu, Y. et al. Regulating electron–hole separation to promote photocatalytic H₂ evolution activity of nanoconfined Ru/MXene/TiO₂ catalysts. *ACS Nano* **14**, 14181–14189 (2020).
- Li, W. et al. Exploiting Ru-induced lattice strain in CoRu nanoalloys for robust bifunctional hydrogen production. *Angew. Chem. Int. Ed.* **60**, 3290–3298 (2021).
- Fu, F. et al. Highly selective and sharp volcano-type synergistic Ni₂Pt@ZIF-8 catalyzed hydrogen evolution from ammonia borane hydrolysis. *J. Am. Chem. Soc.* **140**, 10034–10042 (2018).
- Karaca, T., Sevim, M. & Metin, Ö. Facile synthesis of monodisperse copper–platinum alloy nanoparticles and their superb catalysis in the hydrolytic dehydrogenation of ammonia borane and hydrazine borane. *ChemCatChem* **9**, 4185–4190 (2017).
- Singh, A. K. & Xu, Q. Synergistic catalysis over bimetallic alloy nanoparticles. *ChemCatChem* **5**, 652–676 (2013).
- Wang, S. et al. Aqueous solution synthesis of Pt–M (M = Fe, Co, Ni) bimetallic nanoparticles and their catalysis for the hydrolytic dehydrogenation of ammonia borane. *ACS Appl. Mater. Interfaces* **6**, 12429–12435 (2014).
- Li, J. et al. Highly active and stable metal single-atom catalysts achieved by strong electronic metal–support interactions. *J. Am. Chem. Soc.* **141**, 14515–14519 (2019).
- Chen, W. et al. Synergistic Pt–WO₃ dual active sites to boost hydrogen production from ammonia borane. *iScience* **23**, 100922 (2020).
- Ren, X. et al. Promoting effect of heterostructured NiO/Ni on Pt nanocatalysts toward catalytic hydrolysis of ammonia borane. *J. Phys. Chem. Lett.* **10**, 7374–7382 (2019).
- Zhang, J. et al. Synergistic effects in atomic-layer-deposited PtCo_x/CNTs catalysts enhancing hydrolytic dehydrogenation of ammonia borane. *Appl. Catal. B: Environ.* **235**, 256–263 (2018).
- Ge, Y. et al. PtNi/NiO clusters coated by hollow silica: novel design for highly efficient hydrogen production from ammonia–borane. *ACS Appl. Mater. Interfaces* **9**, 3749–3756 (2017).
- Yao, Q., Shi, Y., Zhang, X., Chen, X. & Lu, Z. Facile synthesis of platinum–cerium(IV) oxide hybrids arched on reduced graphene oxide catalyst in reverse micelles with high activity and durability for hydrolysis of ammonia borane. *Chem. Asian J.* **11**, 3251–3257 (2016).
- Chen, J., Lu, Z., Yao, Q., Feng, G. & Luo, Y. Complete dehydrogenation of N₂H₄BH₃ with NiM–Cr₂O₃ (M = Pt, Rh, and Ir) hybrid nanoparticles. *J. Mater. Chem. A* **6**, 20746–20752 (2018).
- Xu, D. et al. Pt nanoparticles immobilized in mesoporous silica-coated magnetic nanocapsules: a non-leaching catalyst for hydrogen generation from hydrolysis of ammonia borane. *Int. J. Hydrog. Energy* **42**, 27034–27042 (2017).
- Zhou, Q. & Xu, C. Nanoporous PtCo/Co₃O₄ composites with high catalytic activities toward hydrolytic dehydrogenation of ammonia borane. *J. Colloid Interface Sci.* **508**, 542–550 (2017).
- Zhao, B. et al. Pt_xNi_{10–x}O nanoparticles supported on N-doped graphene oxide with a synergetic effect for highly efficient hydrolysis of ammonia borane. *Catal. Sci. Technol.* **7**, 5135–5142 (2017).
- Joo, J. B. et al. Promotion of atomic hydrogen recombination as an alternative to electron trapping for the role of metals in the photocatalytic production of H₂. *Proc. Natl Acad. Sci. USA* **111**, 7942–7947 (2014).
- Roland, U., Braunschweig, T. & Roessner, F. On the nature of spilt-over hydrogen. *J. Mol. Catal. A: Chem.* **127**, 61–84 (1997).
- Conner, W. C. & Falconer, J. L. Spillover in heterogeneous catalysis. *Chem. Rev.* **95**, 759–788 (1995).
- Prins, R. Hydrogen spillover. Facts and fiction. *Chem. Rev.* **112**, 2714–2738 (2012).
- Gao, Z. & Qin, Y. Design and properties of confined nanocatalysts by atomic layer deposition. *Acc. Chem. Res.* **50**, 2309–2316 (2017).
- Zhang, J. et al. Origin of synergistic effects in bicomponent cobalt oxide–platinum catalysts for selective hydrogenation reaction. *Nat. Commun.* **10**, 4166 (2019).
- Xiong, M. et al. In situ tuning of electronic structure of catalysts using controllable hydrogen spillover for enhanced selectivity. *Nat. Commun.* **11**, 4773 (2020).
- Liu, X. et al. Activation of subnanometric Pt on Cu-modified CeO₂ via redox-coupled atomic layer deposition for CO oxidation. *Nat. Commun.* **11**, 4240 (2020).
- Lei, Y., Lee, S., Low, K. B., Marshall, C. L. & Elam, J. W. Combining electronic and geometric effects of ZnO-promoted Pt nanocatalysts for aqueous phase reforming of 1-propanol. *ACS Catal.* **6**, 3457–3460 (2016).
- Zhang, H. & Marshall, C. L. Atomic layer deposition: catalytic preparation and modification technique for the next generation. *Chin. J. Catal.* **40**, 1311–1323 (2019).
- Marichy, C. & Pinna, N. Atomic layer deposition to materials for gas sensing applications. *Adv. Mater. Interfaces* **3**, 1600335 (2016).
- Hu, Q. et al. The precise decoration of Pt nanoparticles with Fe oxide by atomic layer deposition for the selective hydrogenation of cinnamaldehyde. *Appl. Catal. B: Environ.* **218**, 591–599 (2017).
- Karim, W. et al. Catalyst support effects on hydrogen spillover. *Nature* **541**, 68–71 (2017).
- Jiang, L. et al. Facet engineering accelerates spillover hydrogenation on highly diluted metal nanocatalysts. *Nat. Nanotechnol.* **15**, 848–853 (2020).
- Xiong, M., Gao, Z. & Qin, Y. Spillover in heterogeneous catalysis: new insights and opportunities. *ACS Catal.* **11**, 3159–3172 (2021).
- Wei, J. et al. In situ Raman monitoring and manipulating of interfacial hydrogen spillover by precise fabrication of Au/TiO₂/Pt sandwich structures. *Angew. Chem. Int. Ed.* **59**, 10343–10347 (2020).
- Kalidindi, S. B., Indirani, M. & Jagirdar, B. R. First row transition metal ion-assisted ammonia–borane hydrolysis for hydrogen generation. *Inorg. Chem.* **47**, 7424–7429 (2008).
- Yamada, Y., Yano, K., Xu, Q. & Fukuzumi, S. Cu/Co₃O₄ nanoparticles as catalysts for hydrogen evolution from ammonia borane by hydrolysis. *J. Phys. Chem. C* **114**, 16456–16462 (2010).
- Lu, D. et al. A simple and scalable route to synthesize Co_xCu_{1–x}Co₂O₄@Co_xCu_{1–x}Co₂O₄ yolk–shell microspheres, a high-performance catalyst to hydrolyze ammonia borane for hydrogen production. *Small* **15**, 1805460 (2019).
- Hess, N. J. et al. Spectroscopic studies of the phase transition in ammonia borane: Raman spectroscopy of single crystal NH₃BH₃ as a function of temperature from 88 to 330 K. *J. Chem. Phys.* **128**, 034508 (2008).
- Bart, J. C. J. & Vlaic, G. Extended X-ray absorption fine structure studies in catalysis. *Adv. Catal.* **35**, 1–138 (1987).
- Shido, T. & Prins, R. Application of synchrotron radiation to in situ characterization catalysts. *Curr. Opin. Solid State Mater. Sci.* **3**, 330–335 (1998).
- Zhan, W., Zhu, Q. & Xu, Q. Dehydrogenation of ammonia borane by metal nanoparticle catalysts. *ACS Catal.* **6**, 6892–6905 (2016).
- Gudmundsdottir, S., Skulason, E. & Jonsson, H. Reentrant mechanism for associative desorption: H₂/Pt(110)-(1 × 2). *Phys. Rev. Lett.* **108**, 156101 (2012).
- Yu, C. et al. H₂ thermal desorption spectra on Pt(111): a density functional theory and kinetic Monte Carlo simulation study. *Catalysts* **8**, 450 (2018).
- Perdew, J. P., Burke, K. & Ernzerhof, M. Generalized gradient approximation made simple. *Phys. Rev. Lett.* **77**, 3865–3868 (1996).
- Hafner, J. Ab-initio simulations of materials using VASP: density-functional theory and beyond. *J. Comput. Chem.* **29**, 2044–2078 (2008).
- Kresse, G. & Furthmüller, J. Efficiency of ab-initio total energy calculations for metals and semiconductors using a plane-wave basis set. *Comput. Mater. Sci.* **6**, 15–50 (1996).
- Csonka, G. I. et al. Assessing the performance of recent density functionals for bulk solids. *Phys. Rev. B* **79**, 155107 (2009).
- Grimme, S., Antony, J., Ehrlich, S. & Krieg, H. A consistent and accurate ab initio parametrization of density functional dispersion correction (DFT-D) for the 94 elements H–Pu. *J. Chem. Phys.* **132**, 154104 (2010).
- Grimme, S., Ehrlich, S. & Goerigk, L. Effect of the damping function in dispersion corrected density functional theory. *J. Comput. Chem.* **32**, 1456–1465 (2011).
- Gutiérrez, G., Taga, A. & Johansson, B. Theoretical structure determination of γ-Al₂O₃. *Phys. Rev. B* **65**, 012101 (2001).
- Mathew, K., Sundaraman, R., Letchworth-Weaver, K., Arias, T. A. & Hennig, R. G. Implicit solvation model for density-functional study of nanocrystal surfaces and reaction pathways. *J. Chem. Phys.* **140**, 084106 (2014).
- Jónsson, H., Mills, G. & Jacobsen, K. W. in *Nudged Elastic Band Method for Finding Minimum Energy Paths of Transitions* 385–404 (World Scientific, 1998).

Acknowledgements

We acknowledge the financial support from the National Natural Science Foundation of China (21773282, Z.G.; U1932131, Z.G.; and U1832208, Y.Q.), National Science Fund for Distinguished Young Scholars (21825204, Y.Q.), the National Key R&D Programme of China (2017YFA0700101, Y.Q.; and 2020YFA0210902, Y.Q.), and Youth Innovation Promotion Association of the Chinese Academy of Sciences (2018208, Z.G.). We are grateful to all staff at the 1W1B beamline of the Beijing Synchrotron Radiation Facility, Institute of High Energy Physics, Chinese Academy of Sciences, and at BL14W1 and BL11B beamlines of the Shanghai Synchrotron Radiation Facility, Shanghai Advanced Research Institute, Chinese Academy of Sciences.

Author contributions

Z.G. synthesized the catalysts and performed the activity tests. G.W., Z.L., M.X., J.M., and Z.J. helped to perform or provide the XANES measurement. T.L. performed the theoretical calculation. L.W. and S.X. assisted in the synthesis and characterizations of the catalysts. Z.G. and Y.Q. conceived the idea, supervised the work, and wrote the manuscript. All authors contributed to the manuscript.

Competing interests

The authors declare no competing interests.

Additional information

Supplementary information The online version contains supplementary material available at <https://doi.org/10.1038/s41467-021-27785-5>.

Correspondence and requests for materials should be addressed to Zhe Gao or Yong Qin.

Peer review information *Nature Communications* thanks Niall English and the other, anonymous, reviewer for their contribution to the peer review of this work.

Reprints and permission information is available at <http://www.nature.com/reprints>

Publisher's note Springer Nature remains neutral with regard to jurisdictional claims in published maps and institutional affiliations.



Open Access This article is licensed under a Creative Commons Attribution 4.0 International License, which permits use, sharing, adaptation, distribution and reproduction in any medium or format, as long as you give appropriate credit to the original author(s) and the source, provide a link to the Creative Commons license, and indicate if changes were made. The images or other third party material in this article are included in the article's Creative Commons license, unless indicated otherwise in a credit line to the material. If material is not included in the article's Creative Commons license and your intended use is not permitted by statutory regulation or exceeds the permitted use, you will need to obtain permission directly from the copyright holder. To view a copy of this license, visit <http://creativecommons.org/licenses/by/4.0/>.

© The Author(s) 2022